

Physical: Full-length

High-resolution low-dose scanning transmission electron microscopy

James P. Buban^{1,*}, Quentin Ramasse², Bryant Gipson^{1,5},
Nigel D. Browning^{3,4} and Henning Stahlberg^{1,5}

¹Department of Molecular and Cellular Biology, College of Biological Sciences, University of California at Davis, 1 Shields Ave, Davis, ²Lawrence Berkeley National Laboratory, Berkeley, ³Department of Chemical and Materials Science, University of California at Davis, 1 Shields Ave, Davis, ⁴Materials Science and Technology Division, Chemistry, Materials, Earth and Life Sciences Directorate, Lawrence Livermore National Laboratory, P.O. Box 808; L-356 Livermore, CA 94550, USA and ⁵Present address: C-CINA, Biozentrum, University Basel, 4058 Basel, Switzerland

*To whom correspondence should be addressed. E-mail: james.buban@gmail.com

Abstract During the past two decades instrumentation in scanning transmission electron microscopy (STEM) has pushed toward higher intensity electron probes to increase the signal-to-noise ratio of recorded images. While this is suitable for robust specimens, biological specimens require a much reduced electron dose for high-resolution imaging. We describe here protocols for low-dose STEM image recording with a conventional field-emission gun STEM, while maintaining the high-resolution capability of the instrument. Our findings show that a combination of reduced pixel dwell time and reduced gun current can achieve radiation doses comparable to low-dose TEM.

Keywords STEM, low-dose, aberration correction

Received 11 February 2009, accepted 24 September 2009, online 14 November 2009

Introduction

Over the past two decades, scanning transmission electron microscopy (STEM) has been shown to be extremely powerful in revealing information on materials at the atomic level [1–3]. To a first approximation, the resolution in the STEM is directly related to the size of the electron probe—a smaller probe corresponds to a higher spatial resolution. However, decreasing the probe size and increasing the spatial resolution has a consequence; it reduces the beam current and thus reduces the signal-to-noise ratio in the image. This creates difficulties in performing high-resolution experiments that are compounded by the fact that the two most popular techniques in STEM, high-angle angular dark-field (HAADF) imaging and electron energy loss spectroscopy (EELS), inherently only collect a fraction of the scattered electrons. Therefore, much of the recent progress in

STEM has focused on increasing the beam current in the small probe. In this regard, improvements in field-emission guns (FEGs) and the incorporation of spherical aberration (Cs) correctors have increased the beam current density substantially [4,5].

These instrument developments now allow HAADF and EELS spectrum images to be obtained with an impressively high signal-to-noise ratio (SNR) from beam-resistant specimens. However, an unfortunate consequence of the high beam current density is that the techniques are only viable if the specimen can tolerate a very high radiation dose. High radiation dose has devastating consequences for specimens such as zeolites, catalysts and biological samples. Catalysts and zeolites are believed to damage at doses on the order of $100 \text{ e}^-/\text{\AA}^2$ [6]. For biological samples, data collection by transmission electron microscopy (TEM) requires

electron doses $<5 \text{ e}^-/\text{\AA}^2$ with specimens kept at liquid nitrogen temperature, or at doses $<20 \text{ e}^-/\text{\AA}^2$ with sugar-embedded specimens that are at liquid helium temperature (i.e. in the absence of water [7]), if data $<1 \text{ nm}$ resolution are to be recorded. To bring the benefits of high-resolution STEM imaging to the study of these specimens, the development of low-dose electron techniques is imperative.

Much of the development of low-dose microscopy has arisen through the desire to observe beam-sensitive biological specimens at high resolution [8]. Low-dose TEM can reduce the total electron dose to $1\text{--}10 \text{ e}/\text{\AA}^2$, while maintaining a resolution of up to 1.6 \AA [9]. Success of this technique has been demonstrated by high-resolution images of membrane proteins [7,10–13]. Low-dose STEM, on the other hand, is routinely used for low-resolution mass measurements of beam-sensitive biological specimens (recently reviewed in [14]). However, unlike TEM, high-resolution low-dose STEM has not, to date, been successfully developed [15,16].

In the field of materials science, STEM is becoming a widely used high-resolution technique due to many of the advantages it has over conventional TEM, such as imaging with chemical sensitivity, higher resolution and relative ease of image interpretability. It would be a great advancement to retain the benefits of STEM while imaging beam-sensitive materials. For example, catalysts typically damage easily under the electron beam and atomic resolution images have only been obtained for the most robust of catalyst systems [3]. The ability to routinely image the position of metal atoms in beam-sensitive catalysts would be a great step forward in understanding these systems. Also, low-dose STEM could be a way for biological EM to take advantage of the improved contrast transfer function of Cs-corrected microscopy, as the defocus could be dynamically re-adjusted to account for the height change for tilted specimens.

Here, we investigate practical ways to develop a high-resolution low-dose STEM technique and discuss some of the issues that need to be resolved to maximize efficiency. Two simple ways to reduce the dosage in the STEM is to decrease the pixel dwell time and to reduce the beam current density, which are parameters that can be adjusted on any STEM instrument. We report preliminary results for low-dose STEM after adjusting these parameters with a

SrTiO₃ test specimen. We discuss artifacts that easily arise from low-dose imaging, ideal image acquisition conditions and possibilities for dedicated low-dose instrumentation. Additionally, we discuss previously developed image reconstruction methods that are expected to be useful for obtaining high-resolution spatial information from low-dose STEM images.

Methods

Images were acquired using a JEOL JEM-2100F/Cs STEM/TEM with a retro-fitted CEOS Cs corrector at the University of Tokyo. After Cs correction, the probe diameter was $\sim 1.0 \text{ \AA}$. A reading of the electron beam current at normal operating conditions was measured at 50 pA using the ammeter attached to the small phosphorus-viewing screen. For conventional high-dose STEM operation, the JEM-2100F is typically operated with a gun extraction voltage (A1) of $2.8\text{--}3.2 \text{ kV}$, and an electrostatic gun lens voltage (A2) between 6.8 and 7.3 kV . To record images with a reduced beam current, A1 and A2 were reduced to 0.9 kV and 6.2 kV , respectively. Images were obtained using an annular dark-field (ADF) detector with an inner cutoff angle of $\sim 30 \text{ mrad}$, corresponding to low-angle annular dark-field (LAADF) imaging. For all image acquisitions, the accelerating voltage was 200 kV and the ADF detector was the standard JEOL YAG scintillator. This small inner cutoff angle was used in an attempt to increase the SNR in acquired images. The Gatan Digiscan 688 system was used as the scan driver, which was controlled by the Gatan Digital Micrograph software package. The test specimen was a single crystal of SrTiO₃.

Results

Figure 1a shows an image of SrTiO₃ [001] taken under typical high-dose imaging conditions of the Cs-corrected STEM. Here, the imaging conditions are a beam current of $\sim 50 \text{ pA}$, a pixel dwell time of $20 \text{ }\mu\text{s}/\text{pixel}$ and a pixel size of 0.05 \AA^2 . These imaging conditions correspond to a radiation dose of $\sim 1.0 \times 10^8 \text{ e}^-/\text{\AA}^2$. The calculated power spectrum shows clearly visible diffraction spots at 1.4 \AA resolution, as expected for the Cs-corrected JEOL JEM-2100F/Cs. However, the electron dose is ~ 10 million times too high for most biological specimens.

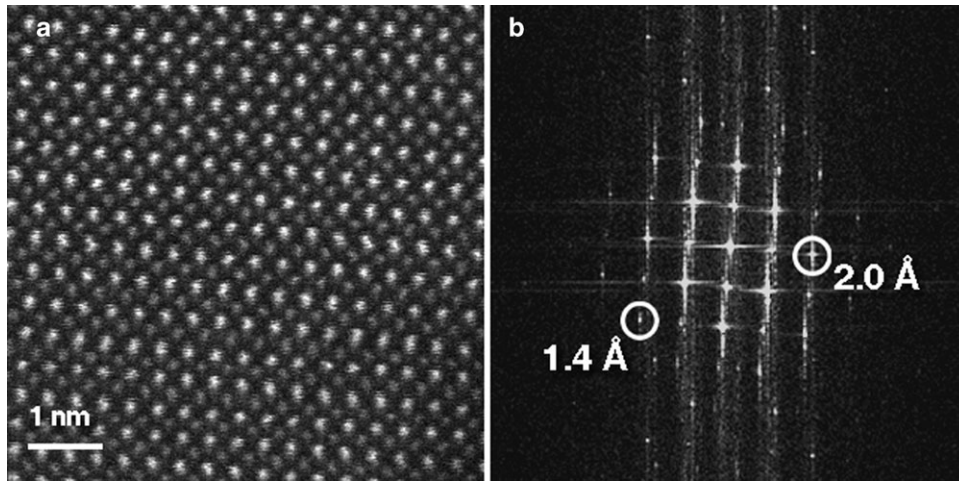


Fig. 1. Standard STEM imaging of SrTiO₃ [001]. (a) Raw image acquired with a Cs-corrected JEOL 2100F with a radiation dosage of $\sim 1 \times 10^8$ e⁻/Å². (b) Fourier transform shows reflections corresponding to a resolution of 1.4 Å.

The most straightforward way to reduce the electron dose during image acquisition in STEM is to reduce the pixel dwell time (i.e. increasing the STEM scanning speed). The Gatan Digiscan system allows the dwell time to be reduced to a minimum of 0.5 μs/pixel. In the STEM, magnification corresponds to changing the pixel size. We chose a magnification to give a pixel size of 0.3 Å². Figure 2a shows an image of SrTiO₃ taken with a dwell time of 0.5 μs/pixel with a typical probe current of ~50 pA. The specimen is exposed to a total radiation dose estimated to be 450 e⁻/Å². A close inspection of the image, however, reveals a streaking artifact parallel to the scan direction. The power spectrum and Fourier-filtered image are shown in Fig. 2b and c, respectively. Fourier filtering was done by masking the Fourier transform spots, using a mask radius of 15 pixels. Noticeable streaking is observed in the raw image, which influences the anisotropic background noise (see the Discussion section). We believe that the observed streaking artifact is caused by a slow reaction time of the employed photomultiplier or read-out electronics, which lead to an anisotropic smearing out of individual signal peaks. An additional artifact that contributes to the anisotropic background is a random horizontal offset of scan lines (see the Discussion section).

This streaking effect can be significantly reduced by increasing the dwell time, i.e. scanning slower. Using the JEOL JEM-2100F/Cs, the streaking effect was noticeably reduced when images were recorded

with a dwell time of 2.0 μs/pixel. However, the 4-fold increase in the dwell time would increase the electron dose from ~ 450 e⁻/Å² (Fig. 2) to ~ 1800 e⁻/Å². Since beam-sensitive specimens often require imaging with much lower electron doses, additional dose reduction is required. We achieve this by decreasing the probe current. Figure 3a shows an image of SrTiO₃, that was recorded with a dwell time of 2.0 μs/pixel and a pixel size of 0.11 Å², while using a probe current of only ~4% of the current used for the image in Fig. 1. The new probe current was confirmed by comparing the reduced probe current value with the original probe current at full emission using the ammeter located on the small phosphorus-viewing screen. The scan artifacts are noticeably less in both the image and the power spectrum, and the apparent resolution is increased with only a small increase in the total electron dose, estimated to be 220 e⁻/Å². In the power spectrum (Fig. 3b), one can see spots at 1.4 Å, which is close to the expected resolution limit of 1.0 Å for the Cs_s-corrected JEOL 2100F/Cs.

Next, we reduced the electron dose to ~ 15 e⁻/Å² by lowering the probe current further to only ~2% of the probe current at full emission (corresponding to a current of ~1 pA) and by decreasing the scan speed to 1.0 μs/pixel and increasing the pixel size to 0.4 Å². An example image is shown in Fig. 4a. The SNR of the resulting real-space image is so low that the naked eye does not discern any structural information in this image. Nevertheless, near atomic

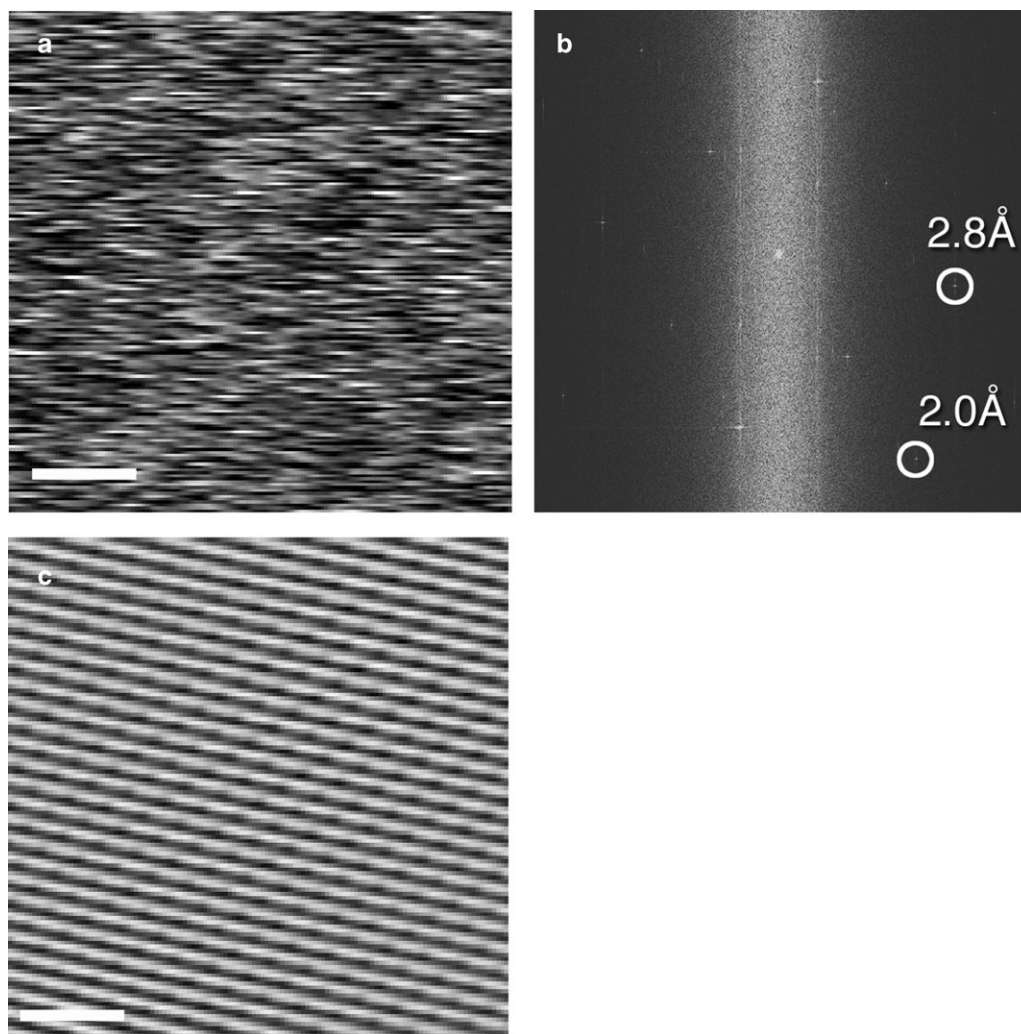


Fig. 2. (a) A (cropped) image of SrTiO₃ [001] taken with a dwell time of 0.5 $\mu\text{s}/\text{pixel}$, a pixel size of 0.3 \AA^2 and a typical gun current of ~ 50 pA, yielding an estimated radiation dose of ~ 450 $\text{e}^-/\text{\AA}^2$. Although atomic planes can be seen faintly in the raw image, a streaking effect parallel to the scan direction is also noticeable. (b) The cropped power spectrum shows higher order reflections at 2.0 \AA . (c) The Fourier-filtered image. The scale bars in (a) and (c) correspond to 2 nm.

resolution features can still be documented in the power spectrum and Fourier-filtered image (Fig. 4b and c). Spots at 3.95 \AA and 2.8 \AA can be clearly seen in the calculated power spectrum of the non-processed image. On increasing the scan speed to 2.0 $\mu\text{s}/\text{pixel}$ (and consequently doubling the dose to ~ 30 $\text{e}^-/\text{\AA}^2$), the power spectrum of the recorded image showed clearly visible diffraction spots at 2.0 \AA resolution (data not shown). Lowering the probe current $< 2\%$ resulted in images that had no discernable features in the power spectrum.

To compare performance with a different machine, STEM images were also recorded with an NION aberration-corrected VG-5 at Lawrence Berkeley Na-

tional Laboratories (Fig. 5). The specimen used for these images was a GaAs thin film containing a layer of AlAs. High-speed scans from that microscope also show the streaking artifact describe above, which presumably is caused by a slow reaction of the read-out elements. In addition, scans at a pixel dwell time of 0.5 μs show a non-constant scan speed, resulting in a compression of the left edge of the recorded images. The pixel size is ~ 0.1 \AA^2 and the probe current was close to 1 pA, which gives a dosage of ~ 30 $\text{e}^-/\text{\AA}^2$. Computational analysis showed that at the beginning of each scan line, the VG-5 electron probe was up to 30% faster, then decelerated during the first half of the scan line, before attaining constant speed for the

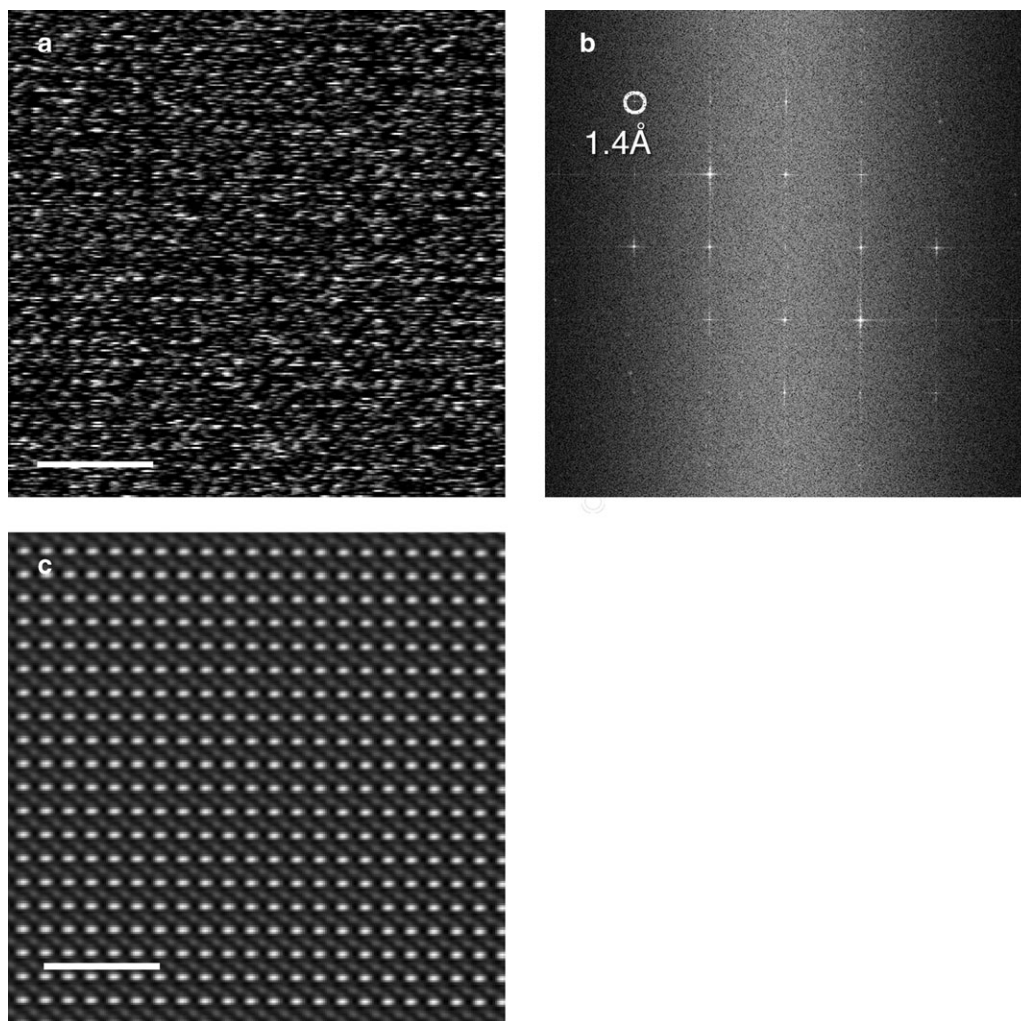


Fig. 3. (a) Raw image of SrTiO₃ [001] taken with a dwell time of 2.0 $\mu\text{s}/\text{pixel}$ and a pixel area of 0.11 \AA^2 , using a gun current of 2 pA, which gives a dosage of $\sim 220 \text{ e}^- \text{\AA}^{-2}$. The streaking affect is reduced in both the image and the power spectrum (b). (c) All images have been cropped to show detail. The scale bars in (a) and (c) correspond to 2 nm.

second half of the scan lines (Fig. 5d). This artifact can easily be computationally corrected, as shown in Fig. 5c.

Discussion

The resolution of an acquired image can be measured by one of several methods, which we briefly summarize here. A direct way to estimate the resolution in any image is to visually inspect the real-space image and determine the closest proximity of peaks that are separated by a lower image intensity of 66% of the peak intensity or less. This method, however, fails when the images exhibit a low SNR, as apparently separated peaks might be random noise fluctuations within the same structural peak. For

such cases, over the last 30 years a number of methods were developed to extract high-resolution data from noisy low-dose TEM images of biological samples. ‘Resolution’, in this context, refers to the resolution of the final reconstruction or processed image. In the case of an image with a periodic signal such as that from crystalline specimen, the calculated power spectrum can be inspected for the presence of diffraction peaks. A very simple resolution definition can then be established by searching for peaks in the power spectrum that lie on the expected crystal lattice position and have an intensity of at least a few times the standard deviation of the noise background in that resolution band. Such peaks are likely caused by a true signal, and the image resolution can be defined to be equal to the distance

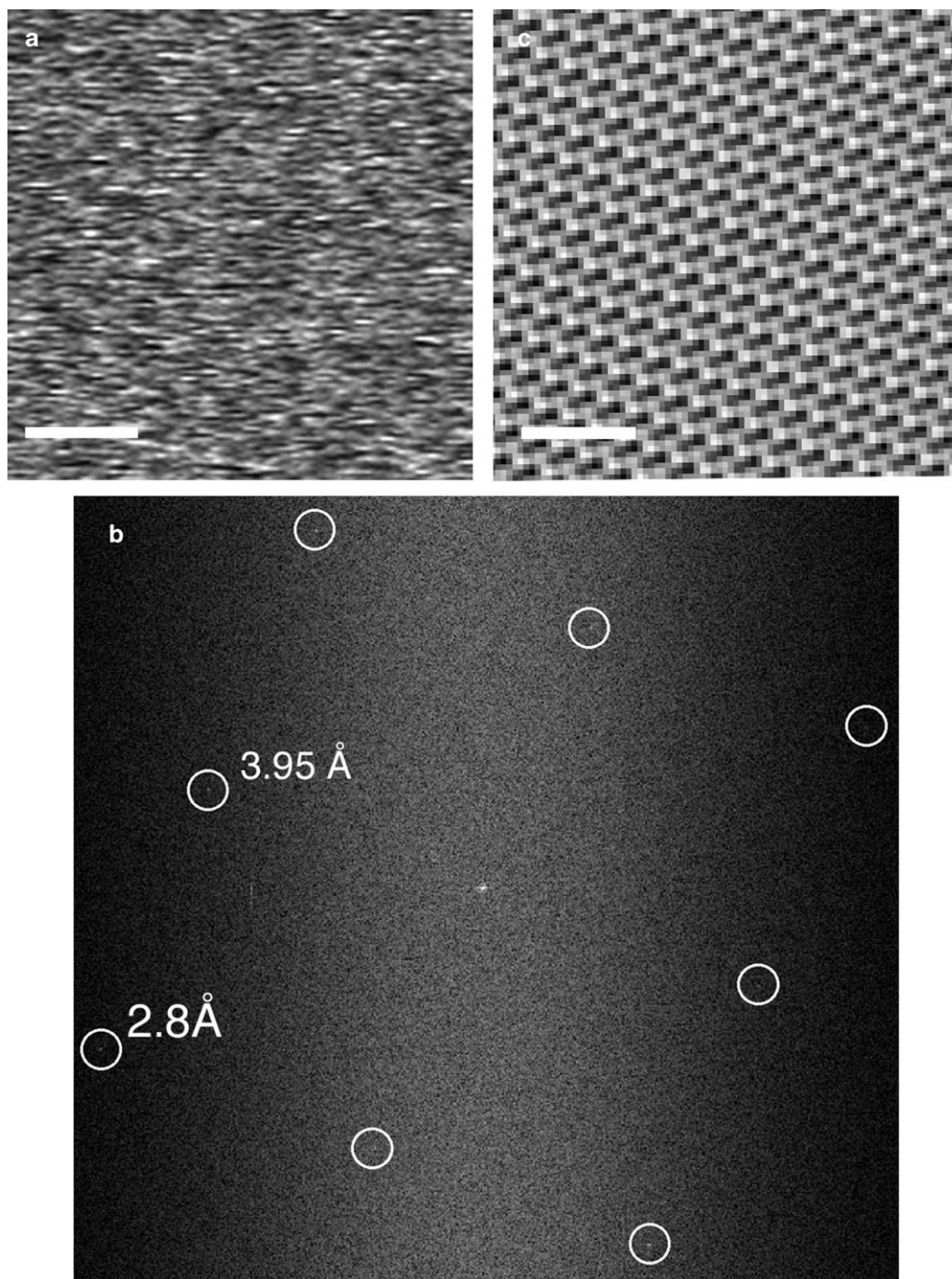


Fig. 4. (a) Raw image of SrTiO_3 [001] obtained with a gun current of 1 pA, a pixel dwell time of $1.0 \mu\text{s}$ and a pixel size of 0.4 \AA^2 . The dosage is estimated to be $\sim 15 \text{ e}^-/\text{\AA}^2$. The power spectrum (b) shows reflections at 2.8 \AA with corresponding lattice fringes seen in the Fourier-filtered image (c). All images have been cropped to show detail. The scale bars in (a) and (c) correspond to 1 nm.

corresponding to the highest order reciprocal lattice point. Since our acquired images were of crystalline specimens, we will use this as our definition of resolution for our discussion.

The goal of low-dose STEM is to image beam-sensitive specimens at a resolution comparable to low-dose TEM. Our results of images with a reso-

lution of 2.0 \AA at a dose of $\sim 20 \text{ e}^-/\text{\AA}^2$ should be suitable for a large range of beam-sensitive material specimens such as catalysts and zeolites. As many of these specimens contain heavier scatters, the SNR should be similar to the current results for SrTiO_3 , especially for specimens with long-range order. Single-particle image analysis techniques (see

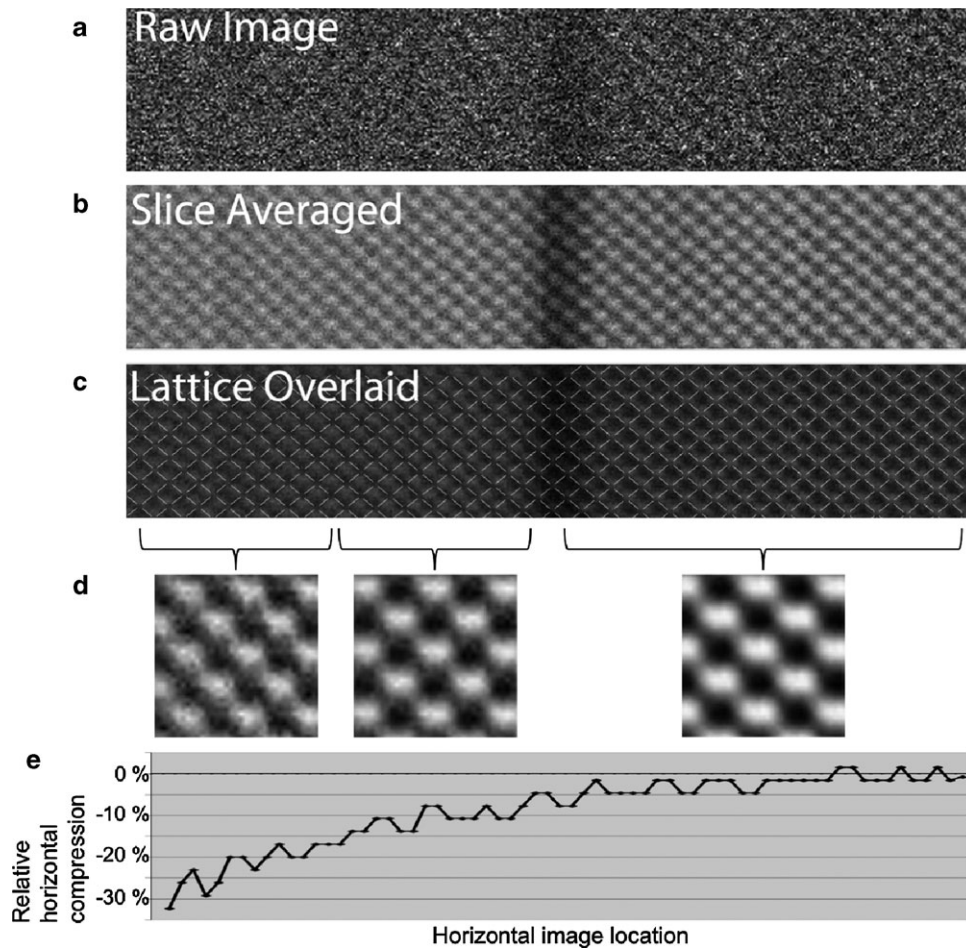


Fig. 5. An example of artifacts from a high-speed low-dose HAADF images of GaAs/AlAs recorded on a NION-corrected VG-5 in LBNL. (a) The horizontal slice of the raw image recorded with a pixel dwell time of $0.5 \mu\text{s}$, a pixel size of $\sim 0.1 \text{ \AA}^2$ and a beam current of close to 1 pA, which gives a dosage of $\sim 30 \text{ e}^-/\text{\AA}^2$. The darker vertical area corresponds to the AlAs layer. (b) An average image of several horizontal slices that were aligned via cross-correlation. (c) The same as in (b), with an overlaid lattice from the right end of the image, to indicate the compression on the left end. (d) Cross-correlational averages of several crystal unit cell areas from the indicated image regions. The right region shows no compression, the image shows clearly resolved dumb-bells. The mid-left region shows horizontal compression and a worse signal-to-noise ratio. The left region shows strong compression which could only be averaged into a noisy map of the lowest signal-to-noise ratio. (e) The relative horizontal compression of the imaged unit cells with respect to the dimensions of the unit cells on the right end of the image. This graph documents up to 30% compression (i.e. faster scan speed) at the beginning of scan lines, with respect to the end of the scan lines. Corrective horizontal stretching via computer image processing could compensate for this artifact.

below) may prove useful for specimens that do not have such extended order such as nano-particles or defects. For biological specimens, achieving an instrument resolution of 2 \AA or better at a dose of $< 10 \text{ e}^-/\text{\AA}^2$ is necessary to be competitive with low-dose TEM.

As can be seen in above images, as the dose in STEM decreases, the noise in the images continues to increase until no high-resolution features can be seen in the raw image. However, the power spectrum shows that structural information is still contained in these images. Thus, high-resolution information is still contained in the images. When a number of

repeated units are present in a specimen, the Rose equation, which estimates the image resolution as a function of signal, can be modified to $d \geq 5/C\sqrt{fkN}$, where d is the resolution, C is the contrast, N is the number of electrons/ \AA^2 , f is the efficiency and k is the number of unit cells [17].

The modified Rose equation states that the resolution of the information in the image depends on the number of identical unit cells in the image. It is therefore advantageous to acquire images as large as possible in order to increase the number of unit cells that can be averaged into one representative map. We can make a rough comparison of this

theoretical limit with the experimental results from our STEM data. We use a value of 0.05 for the contrast C , which is thought to be a good lower bound for the minimum amount of contrast necessary to be discernable [17]. A value of 0.05 was used for the efficiency f , which means we expect at least 5% of the electrons incident upon the specimen to be scattered to angles high enough to reach the DF detector, and for the number of units cells k , we used a value of 9000, which corresponds to the number of unit cells that is present in an image of 4000×4000 pixels (comparable to the size of the lose dose images acquired in this paper) with a unit cell width of 4 \AA (as is the case for SrTiO_3) and a pixel width of 0.3 \AA . With these parameters, we found that a resolution of 1.3 \AA should be obtainable at a dose of $0.7 \text{ e}^-/\text{\AA}^2$. The current experimental data required much higher doses than the Rose equation suggests. This does cause one to suspect that there is room to improve the resolution.

The very short dwell time used for the low-dose images may be one cause for the experimental resolution being poorer than expected. As noted earlier, we found a smearing of the low-dose images along individual scan lines. We believe this to arise from the finite detector response time, which is on the order of a microsecond. Thus, short dwell times cause this smearing effect to become significant. As a rough approximation, we can think of the effect of the response function as a decay function adding a tail to the object functions along the scan direction. This would act as a blurring effect and eliminate the high-frequency noise. In turn, this reduces the intensity of the noise at the left and right sides of the power spectrum. Inspecting the images reveals a blurring width of ~ 3 pixels for $1 \mu\text{s}/\text{pixel}$ dwell times and $\sim 5\text{--}6$ pixels for $0.5 \mu\text{s}/\text{pixel}$ dwell times.

More importantly, high-resolution STEM images almost always have small local shifting of pixels along the scan direction that causes atomic columns to appear 'jittery'. For example, regions of intensity corresponding to the location of an atomic column will often appear as circles that have been sliced along the scan direction and shifted randomly about a mean position. The magnitude of these shifts is rarely more than 2–3 pixels with respect to nearest neighbor scan lines. These shifts often result in the presence of vertical streaks in the power spectrum. Because

of the oscillatory nature of the jitter, we believe the likely source to be stray AC fields. STEM images are typically acquired with a large amount of over-sampling, so that the resulting pixel sizes are much smaller than the probe size or resolution of the microscope. In the case of high-resolution imaging, the pixel width will be on the order of 0.01 nm or less (a small fraction of the resolution limit). Depending on the source of stray fields and its way to affect the scan electronics, the error corresponding to these local scan line offsets might be proportional to the pixel size and therefore not affect image resolution, which is most likely why this issue is normally ignored. However, in our case, the pixel width is very close to the resolution limit (for example Fig. 4 has pixel widths of 0.7 \AA), so that local scan line shifts of up to 3 pixels corresponds to relatively large errors. With these shifts present, we cannot expect to achieve a resolution greater than this error, which not only explains why our low-dose images attain a relatively poor resolution, but also demonstrates why the resolution of the image in Fig. 3 with a pixel width of 0.3 \AA is much higher than the image in Fig. 2 acquired with a pixel width of 0.7 \AA . To our knowledge, the only way to fix this problem would be to decrease the pixel size, remove the sources of the stray fields (if they can be located) or improve the shielding in the scan system to block these fields.

The simplest approach to reducing the discrepancy between the resolution that we obtained experimentally and the resolution limit given by the modified Rose equation would be decreasing the pixel size and/or increasing the pixel dwell time. However, either of these two remedies will increase the electron dose. Thus, it is necessary to reduce the gun current to achieve the lowest doses. However, lowering the gun current using the gun lenses causes practical difficulties. As the current is lowered, viewing the Ronchigram becomes difficult, if not impossible. Thus, aligning the microscope, or even confirming that the microscope is aligned, is no longer achievable. Due to the low SNR, it is imperative that the microscope is at optimal alignment. As mentioned above, we were unable to obtain images with any features in the power spectrum when the probe current was lowered to less than 2% of the typical current probe current at full emission. Therefore, in order to achieve doses lower than $10\text{--}20 \text{ e}^-/\text{\AA}^2$, it is desirable

to find a way to switch between a low gun current mode and a standard mode without affecting the alignment of the gun or any lenses.

One way to address this issue may be to develop a beam dimmer that operates in the high-frequency time domain. This could be implemented by using electrostatic plates that rapidly shunt the electron beam between on- and off-axis positions so that the total beam current is reduced. The best method would be shunting the beam synchronously with the dwell time so that the beam is switched on axis for only a fraction of a microsecond per pixel. Another, perhaps easier, method may be to continuously oscillate the beam at a frequency much higher than the pixel repetition rate between the on- and off-axis positions and give the operator control over what fraction of the time the beam is actually on axis. Either of these techniques would allow the operator to perform alignment adjustments with a bright electron beam and then dim the gun back to low-dose mode without any additional alterations to the lenses.

One of the key issues with low-dose imaging is the amount of noise in the images and how this affects the image resolution. Of course the resolution limit due to aberrations or environmental instabilities will not be affected by changes in the electron doses. From the above discussion it is apparent that the Rose equation gives a bound on the spatial frequencies that can contribute to interpretable image contrast. On the other hand, the modified Rose equation suggests that appropriate statistical methods may maximize the amount of extractable information at high resolution. In the case of crystalline specimens, a suitable tool is Fourier filtering combined with correcting any distortions in the image. These distortions may arise from the crystal itself in the case of biological 2D crystals, which often show poor ordering, or from instabilities in the scan system, as demonstrated above and elsewhere [18,19]. Various groups have developed techniques and software packages to correct or ‘unbend’ distorted lattices [20–23]. With smaller images that do not show enough crystal lattice unit cells to produce strong diffraction peaks, the weaker spots in the calculated Fourier transformation could still contain true and valuable signal data, despite being closer to the background noise. Numerical extraction of the values for amplitude and phase of the diffraction peaks then

allows comparing them with measurements from other images, or in the case of crystallographic symmetry in the image, these peak values can be compared with those of symmetry-related peaks. A commonly used resolution criterion is then the phase residual during averaging of symmetry or otherwise related peak values.

Specimens containing small clusters of atoms such as catalysts or single molecules or proteins supported by a carbon film can be modeled as identical particles at random locations and orientations. In this case, comparisons can be done between boxed regions from the real-space image containing a single particle of interest. These boxed regions can then be aligned, classified and averaged. The resulting class averages can be compared with other averages from other image locations, other images or symmetry-related mirrored or rotated copies of themselves. A versatile software package for such analysis is for example found in the SPIDER software [24]. Various mathematical tools are available to evaluate the image resolution. The most commonly used method to measure the resolution of a particle reconstruction that was calculated from a larger number of single-particle images is the Fourier Shell Correlation (FSC) [25]. Other related methods for the resolution determination of a single-particle reconstruction are the spectral signal-to-noise ratio (SSNR) [26,27] and the Q -factor [28,29]. Another resolution estimation is calculated by the program RMEASURE, which does an analysis of the final reconstruction by determining the neighbor correlation of pixels in the Fourier transform of the final reconstruction, to provide an estimate of the resolution of the reconstruction. This algorithm is independent of the method by which the reconstruction was obtained [30].

As a last remark, we note that simultaneous acquisition of bright-field (phase contrast) and dark-field signals can give complementary information [31] and that the combination of these signals could maximize information obtainable in the STEM.

Concluding remarks

We have shown that low-dose STEM is capable of recording high-resolution images. LAADF STEM images at an electron dose of $\sim 15 \text{ e}^-/\text{\AA}^2$ showed interpretable structure information at a resolution of 2.8 \AA . At a higher dose of $\sim 30 \text{ e}^-/\text{\AA}^2$, we obtained

images showing a resolution of 2.0 Å. The employed high-speed scanning resulted in the generation of various image artifacts, such as horizontal peak smearing, off-set of individual scan lines and a variable scan speed. Some of these artifacts in the recorded images can be corrected computationally. Nevertheless, our results also show that there are limitations to the scan speed and probe current reduction, if the instrument alignment should still be possible, and image artifacts are to be minimized. We conclude that a device such as a high-speed stroboscopic beam dimmer is needed for routine low-dose STEM operation. Nevertheless, with currently available instrumentation, atomic resolution imaging is possible with doses on the order of $10^2 \text{ e}^-/\text{Å}^2$.

Funding

This work was in part supported by DOE grant DE-FG02-03ER46057, by the National Institutes of Health (NIGMS) grant U54 GM074929-01 and by the National Science Foundation (NSF) grant MCB 0447860.

Acknowledgements

We thank Professor Yuichi Ikuhara at the University of Tokyo for permission to use the JEOL JEM-2100F/C_s. We also thank Ken Downing and Bob Glaeser for fruitful discussions.

References

- Jesson D E, and Pennycook S J (1995) Incoherent imaging of crystals using thermally scattered electrons. *Proc. R. Soc. London Ser. A* **449**: 273–293.
- Batson P E, Dellby N, and Krivanek O L (2002) Sub-angstrom resolution using aberration corrected electron optics. *Nature* **418**: 617–620.
- Nellist P D, Chisholm M F, Dellby N, Krivanek O L, Murfitt M F, Szilagy Z S, Lupini A R, Borisevich A, Sides W H, and Pennycook S J (2004) Direct sub-angstrom imaging of a crystal lattice. *Science* **305**: 1741–1744.
- Krivanek O L, Nellist P D, Dellby N, Murfitt M F, and Szilagy Z (2003) Towards sub-0.5 Å electron beams. *Ultramic* **96**: 229–237.
- Smith D J (2008) Development of aberration-corrected electron microscopy. *Microsc. Microanal.* **14**: 2–15.
- Pan M, and Crozier P A (1993) Quantitative imaging and diffraction of zeolites using a slow-scan CCD camera. *Ultramic* **52**: 487–498.
- Fujiyoshi Y (1998) The structural study of membrane proteins by electron crystallography. *Adv. Biophys.* **35**: 25–80.
- Glaeser R M (1971) Limitations to significant information in biological electron microscopy as a result of radiation damage. *J. Ultrastruct. Res.* **36**: 466–482.
- Evans J E, Hetherington C, Kirkland A I, Chang L Y, Stahlberg H, and Browning N D (2008) Low-dose aberration corrected cryo-electron microscopy of organic specimens. *Ultramic* **108**: 1636–1644.
- Henderson R, Baldwin J M, Ceska T A, Zemlin F, Beckmann E, and Downing K H (1990) Model for the structure of bacteriorhodopsin based on high-resolution electron cryo-microscopy. *J. Mol. Biol.* **213**: 899–929.
- Gonen T, Cheng Y, Sliz P, Hiroaki Y, Fujiyoshi Y, Harrison S C, and Walz T (2005) Lipid-protein interactions in double-layered two-dimensional AQP0 crystals. *Nature* **438**: 633–638.
- Schmidt-Krey I (2007) Electron crystallography of membrane proteins: two-dimensional crystallization and screening by electron microscopy. *Methods (San Diego, Calif)* **41**: 417–426.
- Gyobu N, Tani K, Hiroaki Y, Kamegawa A, Mitsuoka K, and Fujiyoshi Y (2004) Improved specimen preparation for cryo-electron microscopy using a symmetric carbon sandwich technique. *J. Struct. Biol.* **146**: 325–333.
- Müller S A, and Engel A (2006) Biological scanning transmission electron microscopy: imaging and single molecule mass determination. *Chimia* **60**: 749–753.
- Rez P (2003) Comparison of phase contrast transmission electron microscopy with optimized scanning transmission annular dark field imaging for protein imaging. *Ultramic* **96**: 117–124.
- Henderson R (1995) The potential and limitations of neutrons, electrons and X-rays for atomic resolution microscopy of unstained biological molecules. *Quart. Rev. Biophys.* **28**: 171–193.
- Kuo I A, and Glaeser R M (1975) Development of methodology for low exposure, high resolution electron microscopy of biological specimens. *Ultramic* **1**: 53–66.
- Winkelman G B, Dwyer C, Hudson T S, Nguyen-Manh D, Doblinger M, Satet R L, Hoffmann M J, and Cockayne D J H (2004) Arrangement of rare-earth elements at prismatic grain boundaries in silicon nitride. *Phil. Mag. Lett.* **84**: 755–762.
- Kirkland A I, and Saxton W O (2002) Cation segregation in Nb₁₆W₁₈O₉₄ using high angle annular dark field scanning transmission electron microscopy and image processing. *J. Microsc.* **206**: 1–6.
- Henderson R, and Unwin P N (1975) Three-dimensional model of purple membrane obtained by electron microscopy. *Nature* **257**: 28–32.
- Crowther R A, Henderson R, and Smith J M (1996) MRC image processing programs. *J. Struct. Biol.* **116**: 9–16.
- Gipson B, Zeng X, and Stahlberg H (2007) 2dx merge: data management and merging for 2D crystal images. *J. Struct. Biol.* **160**: 375–384.
- Gipson B, Zeng X, Zhang Z Y, and Stahlberg H (2007) 2dx—user-friendly image processing for 2D crystals. *J. Struct. Biol.* **157**: 64–72.
- Frank J, Radermacher M, Penczek P, Zhu J, Li Y, Ladjadj M, and Leith A (1996) SPIDER and WEB: processing and visualization of images in 3D electron microscopy and related fields. *J. Struct. Biol.* **116**: 190–199.
- Harauz G, and van Heel M. (1986) Exact filters for general geometry 3-dimensional reconstruction. *Optik* **73**: 146–156.
- Unser M, Trus B L, Frank J, and Steven A C (1989) The spectral signal-to-noise ratio resolution criterion: computational efficiency and statistical precision. *Ultramic* **30**: 429–433.
- Unser M, Trus B L, and Steven A C (1987) A new resolution criterion based on spectral signal-to-noise ratios. *Ultramic* **23**: 39–51.
- van Heel M, and Hollenberg J (1980) In: Baumeister W (ed.), *Electron Microscopy at Molecular Dimensions*, pp. 256–260 (Springer, Berlin, New York).
- Kessel M, Radermacher M, and Frank J (1985) The structure of the stalk surface layer of a brine pond microorganism: correlation averaging applied to a double layered lattice structure. *J. Microsc.* **139**: 63–74.
- Sousa D, and Grigorieff N (2007) Ab initio resolution measurement for single particle structures. *J. Struct. Biol.* **157**: 201–210.
- Shibata N, Chisholm M F, Nakamura A, Pennycook S J, Yamamoto T, and Ikuhara Y (2007) Electron microscopy reveals that in aluminum oxide, nonstoichiometric dislocations form on adjacent planes and slip together during high-temperature deformation. *Science* **316**: 82–85.